

Excited-state absorption in ruby, emerald, and MgO:Cr³⁺†

W. M. Fairbank, Jr.,* G. K. Klauminzer,† and A. L. Schawlow

Department of Physics, Stanford University, Stanford, California 94305

(Received 26 August 1974)

Absorption from the metastable 2E and 2T_1 states of Cr³⁺ has been measured in ruby with more precision than in previous experiments and in emerald and MgO:Cr³⁺ for the first time. The sharp 2E , ${}^2T_1 \rightarrow {}^2T_2$ I lines are resolved in these three crystals, as well as the ${}^2E \rightarrow {}^2A_1$ lines in ruby and the ${}^2E \rightarrow {}^2A_2$ lines in ruby and MgO:Cr³⁺. Three excited-state bands are also seen in each crystal. To confirm the assignments of the observed transitions, the energy matrices are diagonalized, and intensity calculations using the closure approximation are made. In particular, the sharp lines in MgO:Cr³⁺ are found to be from the tetragonal vacancy and pair systems rather than the cubic system. The predicted polarization selection rules are experimentally confirmed and, except for the ${}^2E \rightarrow {}^2A_2$ transition, the observed intensities are explained well by theory. This anomalous transition is more than an order of magnitude stronger than predicted by theory in all three crystals.

I. INTRODUCTION

The optical properties of Cr³⁺ ions in various crystal lattices have been a subject of a large amount of research over the last two decades. Most of the experimental work has involved transitions from the 4A_2 ground state. The few experiments which measured excited-state absorption from the metastable 2E and 2T_1 levels have concentrated mainly on ruby.¹⁻⁸ In this paper we report excited-state absorption measurements for ruby, emerald, and MgO:Cr³⁺. Three broad excited-state absorption bands are observed in all three crystals. In addition, detailed measurements are made of the sharp structure in the transitions to the 2T_2 , 2A_1 , and 2A_2 levels. The intensities of the observed transitions are studied theoretically to confirm the assignments and to analyze the source of the strength of these parity-forbidden transitions.

In all three crystals the Cr³⁺ impurity ions enter sites of octahedral coordination. The predominant crystal field is of cubic symmetry, but there are also small even- and odd-parity fields which vary from crystal to crystal. These small fields split the energy levels and break the cubic-symmetry selection rules. By studying several crystals we can compare the effects of different perturbing fields.

The Cr³⁺ ion in ruby (Al₂O₃:Cr³⁺) is in a site of trigonal symmetry C_3 . The even-parity trigonal component T_{2g} results from a stretching of the O²⁻ ions along the C_3 axis. The odd-parity field contains three terms of symmetry type $T_{1u}a_0$, $T_{2u}\chi_0$, and $A_{2u}e_2$. These arise, respectively, from a displacement of the Cr³⁺ along the C_3 axis relative to the octahedron center, a rotation of one triangle of O²⁻ about the C_3 axis relative to the other triangle, and a size reduction of one triangle relative to the other.⁹

The Cr³⁺ ion in emerald [Be₃Al₂(SiO₃)₆:Cr³⁺] is

also in a site of trigonal symmetry, but in this case it is D_3 .^{10,11} In addition to the C_3 axis found in ruby, there are two C_2 symmetry axes perpendicular to it through the chromium ion. In this case the trigonal T_{2g} field results from a compression along the C_3 axis (note that this is the opposite of the extension in ruby so that splittings are reversed with respect to ruby). The only possible odd-parity field is of type $T_{2u}\chi_0$.¹² It could arise from the influence of the SiO₄ tetrahedrons surrounding the Cr³⁺,¹³ or perhaps from a distortion of the octahedron.¹⁴

MgO:Cr³⁺ is both simpler and more complex than ruby and emerald. Most of the ions (81% to 95% in weakly doped crystals)^{15,16} enter sites of purely cubic symmetry. A study of these sites is useful for isolating the effects of the cubic field. The crystal is complicated, however, by the existence of one vacant Mg²⁺ site for every Cr³⁺ ion in order to ensure charge neutrality in the crystal. The vacancies often occur (perhaps for 15% of the ions)¹⁵ in a next-nearest-neighbor Mg site along the Cr-O axes. The chromium ions in these "vacancy" sites experience tetragonal fields of both even and odd parity. A smaller number of Cr³⁺ (4%)¹⁵ have a vacancy in the nearest-neighbor site along one of the [110] axes. These ions experiencing rhombic symmetry have been seen by ESR but have never been positively identified in optical spectra.¹⁵ When the doping is large, sites with pairs of chromium ions or a pair plus a vacancy must also be considered. Predominantly these "pair" sites experience a tetragonal field nearly the same as the vacancy sites. There are also sites of more complicated configuration which are probably responsible for some of the unidentified lines seen in ESR and optical spectra. One can see, therefore, that a wealth of interesting information can be found in the multiplicity of sites in MgO:Cr³⁺. But one must pay the price of having to unravel the various con-

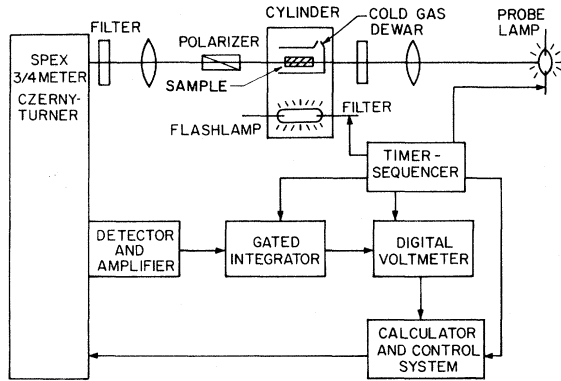


FIG. 1. Apparatus for measuring excited-state absorption in crystals.

tributions of the different sites.

II. EXPERIMENTAL

The excited-state absorption apparatus is shown in Fig. 1. It is similar to previous schemes^{2,4,6} but has some special features which result in better signal-to-noise ratio and resolution than has previously been achieved. Cr^{3+} atoms in various sample crystals are pumped to the lowest excited states (2E and 2T_1) by a flash lamp. A short time later a probe lamp is pulsed to look for absorption from these excited states. Probe light which is transmitted through the sample passes through a spectrometer and is monitored in a sophisticated detector scheme.

The flash lamp (PEK, Xe-14-C-3) was water cooled to allow a repetition rate limited only by sample cooling capacity. The pulse width was 1 msec. The probe lamp was a 300-W Xe short arc (PEK, C-300-6050A) running continuously at rated power and pulsed with 1 J in 15 msec. This lamp and its hydrogen thyratron pulsing circuit were designed to produce light pulses of high reproducibility;

the design and performance of the probe lamp system is described elsewhere.¹⁷ The samples were mounted in a Dewar and cooled with a flow of cold nitrogen or helium gas. The sample could be cooled to 95 K with nitrogen and to 40 K with helium. The various samples used in this study are listed in Table I.

The detectors were an InSb photoconductor (Philco ISC-501B) for the near-infrared, a PIN diode (UDT PIN-10) or a photomultiplier (RCA C31000F) for the visible, and an RCA 1P28 photomultiplier for the ultraviolet. The integrator was of the "boxcar" design¹⁸ modified to reset after each pulse. The dc voltage from the integrator was measured with a digital voltmeter and entered into a Hewlett-Packard 9100A desktop calculator which operates as an on-line computer. The details of the calculator and control system have been described elsewhere.¹⁹ It functions to average the data at a particular wavelength, print and plot the results, and step the spectrometer to the next wavelength position.

The data analysis is as follows: Each piece of absorption data at a single wavelength consists of two intensity measurements, one with the crystal unpumped and one with the crystal pumped, just after the flash lamp has been fired. The calculator averages the ratio of these intensities which are entered at a rate of 15 pairs (15 ratios) per minute. The transmitted intensity in the unpumped case is

$$I_u = I_0 e^{-N_0 \sigma_1 l} \quad (1)$$

When the sample is pumped, the transmission is

$$I_p = I_0 e^{-(N_2 \sigma_2 + N_1 \sigma_1) l} \quad (2)$$

N_1 and N_2 are the number of Cr^{3+} ions in the ground (4A_2) and excited (2E and 2T_1) states, respectively, N_0 is the total ion density, σ_1 and σ_2 are the absorption cross sections for the ground and excited states, and l is the crystal length. We assume

TABLE I. Samples used in this experiment.

Sample	Size	Orientation	Concentration	N (cm^{-3})	Source
Ruby	1 cyl. 3 in. \times $\frac{1}{2}$ -in. diam.	90°	0.044-wt % Cr_2O_3 ^a	1.4×10^{19}	Mueller
	2 cyl. 2 cm \times $\frac{1}{2}$ -in. diam.	90°	0.044-wt % Cr_2O_3 ^a	1.4×10^{19}	Linde
	3 cyl. 3 cm \times $\frac{1}{2}$ -in. diam.	90°	0.021-wt % Cr_2O_3 ^a	6.7×10^{18}	Mueller
	4 cyl. 1 cm \times $\frac{1}{2}$ -in. diam.	0°	nominal 0.05-wt %	1.6×10^{19}	Linde
Emerald	1 slice $\frac{1}{4}$ in. \times $\frac{3}{16}$ in. \times $\frac{1}{16}$ in.	in plane of slice	0.6-wt % Cr^{3+} ^b	1.85×10^{20}	Chatham
$\text{MgO} : \text{Cr}^{3+}$	1 cyl. 3 cm \times $\frac{1}{2}$ -in. diam.	...	0.061-wt % Cr_2O_3 ^c	1.79×10^{19}	Norton
	2 cyl. $\frac{3}{8}$ in. \times $\frac{1}{2}$ -in. diam.	...	0.018-wt % Cr_2O_3 ^d	5.3×10^{18}	Materials Research
	3 cyl. $\frac{3}{8}$ in. \times $\frac{5}{16}$ -in. diam.	...	0.22-wt % Cr_2O_3 ^d	6.4×10^{19}	Norton

^aAnalyzed spectrophotometrically (Ref. 42).

^bSpectrophotometrically referenced to Wood (Ref. 13).

^cAnalyzed by Norton Company.

^dSpectrophotometrically referenced to sample 1. For sample 3, this was consistent with a cubic site spin measurement by Wertz if approximately 50% of the Cr^{3+} ions are in cubic sites.

that $N_1 + N_2 = N_0$ so that the ratio of the two detected intensities is

$$I_u/I_p = e^{N_2(\sigma_2 - \sigma_1)l} \quad (3)$$

It is clear from this equation that to extract σ_2 , both the excited population N_2 and ground-state cross section σ_1 must be known. Solving for σ_2 we get

$$\sigma_2 = \sigma_1 + (1/N_2l) \ln(I_u/I_p) \quad (4)$$

The cross section σ_2 in Eq. (4) is not in general a meaningful cross section because two metastable excited states, each split into several levels, are involved. Absorption from these various levels overlap and cannot be resolved in most cases. Only for some of the sharp-line transitions can cross sections for individual transitions be quoted. Except for these cases the listed cross section σ_2 is therefore the ratio of the total excited-state absorption coefficient

$$\alpha_2 = \sum_i N_i \sigma_i \quad (5)$$

and the excited-state population

$$N_2 = \sum_i N_i \quad (6)$$

N_i are the Boltzmann populations of the metastable excited states. With the exception of the ${}^2T_1 \rightarrow {}^2T_2$ transition, the quoted oscillator strengths in this paper are also not corrected for the Boltzmann populations.

The excited population can be measured by several means,^{2,4,6,20-23} the most successful of which has been to measure a decrease in ground-state absorption upon pumping. Sharp ground-state transitions such as the *B* lines in ruby and emerald are ideal since they are strong and can be distin-

guished easily from overlapping excited absorption. A sharp peak in σ_1 appears as a sharp dip in the raw data, $\ln(I_u/I_p)$. Assuming the excited absorption, σ_2 , is smooth over this small region we can adjust N_2/N_0 in (4) until the peak in σ_1 balances the dip in the raw data, and α_2 is smooth. Using this technique we have measured populations in the (20–40)% range to $\pm 10\%$ of the measurement. For MgO:Cr³⁺ an alternate technique was required, since the *B* lines of the vacancy site are too weak for reliable population measurements. (The *R* lines cannot be used because of strong fluorescence.) This other technique relies on correcting the absorption data. Note from Eq. (3) that the exponent is negative when $\sigma_1 > \sigma_2$. The data are corrected for ground-state population by adding $N_2\sigma_1l$ to the exponent [Eq. (4)]. If N_2 is unknown, a lower limit can be established as that required to make σ_2 positive or zero at all wavelengths. An upper limit can be estimated, for if N_2 is too high the calculated excited absorption appears much like the ground-state curve. Although unappealing, this technique is reasonably effective in practice. For MgO:Cr³⁺ we can bracket the population as between 3.5% and 6%.

It should be noted that the excited absorption can be readily confirmed as arising from the metastable states by observing its decrease as the probe pulse is further delayed from the pump pulse. In all cases the excited absorption accurately followed the lifetime of the metastable states. This procedure can be used to confirm the identity of sharp transitions as will be shown later in the case of MgO:Cr³⁺. Color centers, observed in MgO:Cr³⁺, have lifetimes much longer than the metastable states, and their effect, usually very small, can be eliminated from the data.

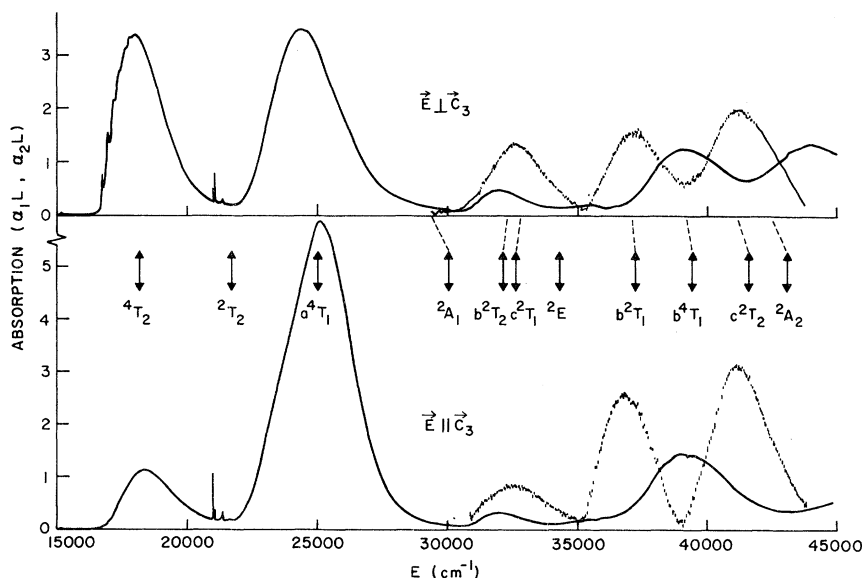


FIG. 2. Ground- and excited-state absorption spectra of ruby (sample 3) at 103 K. The excited-state spectra are shifted by the 2E state energy and normalized to 100% population in the metastable excited states. (The 2A_1 level absorption was measured with sample 1 and normalized to the density and length of sample 3.) The results of energy level calculations are shown.

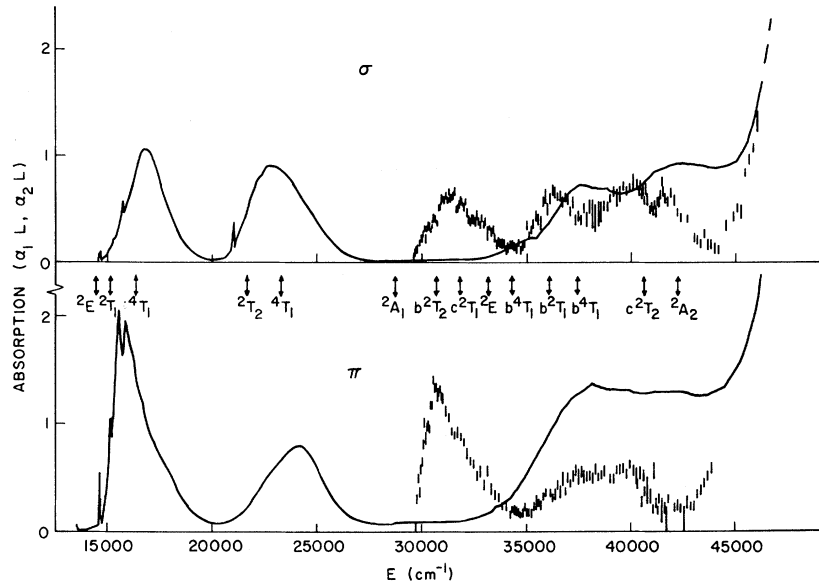


FIG. 3. Ground- and excited-state absorption spectra of emerald at 113 K.

The excited-state absorption coefficients for ruby, emerald, and MgO:Cr^{3+} , along with ground-state absorption curves measured on a Cary 14 spectrophotometer, are shown in Figs. 2-4. The solid line represents the ground-state absorption coefficient. The excited-state absorption coefficient is shown by vertical lines representing individual point-by-point measurements with \pm one standard deviation error bars. As most excited-state absorption arises from the metastable 2E level, the excited-state data have been shifted by the 2E state energy. In this way all energies can be compared relative to the ground-state level. Theoretical level positions from energy-level cal-

culations are also shown. For clarity, excited-state data on lines in the infrared discussed below are omitted from Figs. 2-4.

The outstanding new features of these data are the sharp lines in the high-energy (ultraviolet) portion of the excited-state spectra. In ruby these were observed by Dunn and Francis by photographic means.⁸ Detailed quantitative measurement of the structure of these lines and sidebands is presented here. In Fig. 4 the same type of strong lines are observed in MgO:Cr^{3+} . For emerald in Fig. 3 the lines and sidebands are broadened into a weak band. Theoretical assignment, discussed later, identifies these levels as the $(t_2^2 e) {}^2A_2$ of Cr^{3+} in an

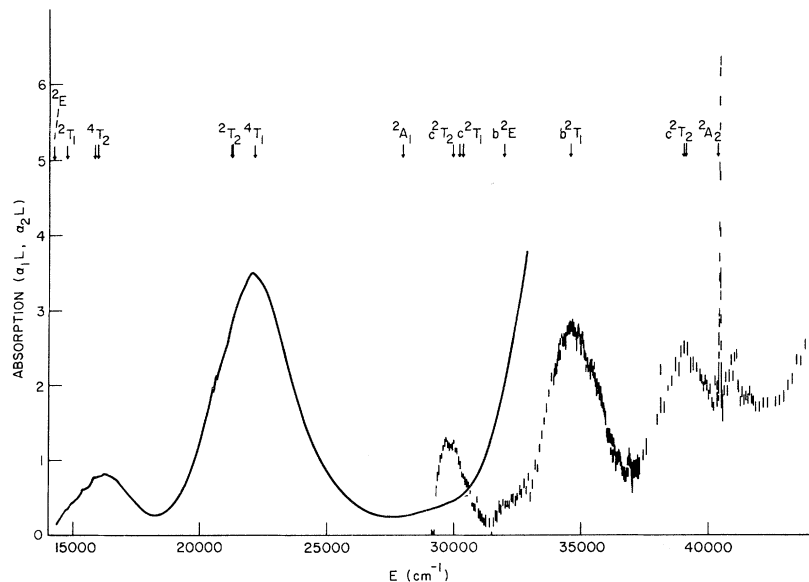


FIG. 4. Ground- and excited-state absorption spectra of MgO:Cr^{3+} (sample 1) at 120 K. The results of the energy level calculations for the cubic system are shown.

TABLE II. Approximate total oscillator strengths of ground- and excited-state transitions in ruby, emerald, and two MgO:Cr³⁺ systems. The calculations for the MgO vacancy system assume 10% of the Cr³⁺ are in the vacancy system in sample 1.

Transition		Ruby	Emerald	MgO (cubic)	MgO (vacancy)
${}^4A_2 \rightarrow {}^4T_2$	σ	2.6×10^{-4}	0.6×10^{-4}	0.3×10^{-4}	
	π	0.8×10^{-4}	1×10^{-4}		
${}^4A_2 \rightarrow {}^4T_1$	σ	4×10^{-4}	0.8×10^{-4}	1.7×10^{-4}	
	π	6×10^{-4}	0.7×10^{-4}		
${}^2E \rightarrow {}^2T_2$	no-phonon lines	5×10^{-6}	7×10^{-6}		3×10^{-6}
${}^2T_1 \rightarrow {}^2T_2$	no-phonon lines	1.4×10^{-4}	$< 2 \times 10^{-4}$		
${}^2E \rightarrow {}^2A_1$	total	1.5×10^{-6}			
	no-phonon	2×10^{-7}			
${}^2E \rightarrow {}^2A_2$	total	5×10^{-5}	$\sim 1 \times 10^{-5}$		9×10^{-5}
	no-phonon	2×10^{-6}			1.3×10^{-5}
${}^2E \rightarrow c^2T_1, b^2T_1$	σ	1.2×10^{-4}	0.5×10^{-4}	0.2×10^{-4}	
	π	0.8×10^{-4}	0.9×10^{-4}		
${}^2E \rightarrow b^2T_1$	σ	1.4×10^{-4}	0.4×10^{-4}	1.0×10^{-4}	
	π	2.1×10^{-4}	0.3×10^{-4}		
${}^2E \rightarrow c^2T_2$	σ	2.1×10^{-4}	0.6×10^{-4}	0.9×10^{-4}	
	π	2.8×10^{-4}	0.35×10^{-4}		

octahedral coordination.

We also observe sharp structure in the excited-state data at lower energies (red light) in ruby.⁸ This is assigned to the $(t_{2e}^2) {}^2A_1$ level. In MgO and emerald ${}^2E \rightarrow {}^2A_1$ absorption is not observed because the predicted wavelength is above 7000 Å, where fluorescence from the sidebands of the *R* line overwhelms excited-state absorption measurements [Eq. (4) is only applicable at wavelengths where there is no fluorescence].

In addition to the lines, three excited bands are seen for all the crystals in Figs. 2–4. These are assigned to other states of the t_{2e}^2 configurations: b^2T_2 and c^2T_1 together unresolved, b^2T_1 , and c^2T_2 . Kushida observed small bumps on the low-energy side of the first band, which he claimed to be the b^2T_2 level.² No such bumps are observed here. His small bump in σ polarization is probably the 2A_1 level absorption, seen here with much better resolution.

The oscillator strengths of the observed excited-state transitions are listed in Table II. In these calculations we have included the proper correction to the oscillator strength due to reduction of the electric field in a medium of refractive index n ²⁴:

$$f = \frac{mc}{\pi N e^2} \left(\frac{9n}{(n^2 + 2)^2} \right) \int k(\nu) d\nu. \quad (7)$$

To compare our data to others¹² who ignore refractive effects, multiply our numbers by 1.66, 1.42, and 1.61 for ruby, emerald, and MgO:Cr³⁺, respectively.

The data which follow are separated into two categories by type of transition which also correspond to distinct wavelength regions. The initial states for all transitions are the metastable $(t_{2e}^2) {}^2E$ and $(t_{2e}^2) {}^2T_1$ levels which are in thermal equilibrium. The first category involves the terminal state $(t_{2e}^2) {}^2T_2$ and appears in the near-infrared; the second involves higher states of configuration (t_{2e}^2) and appears in the visible and ultraviolet regions.

A. Transitions to $(t_{2e}^2) {}^2T_2$

1. Ruby

The appropriate energy levels and eigenfunctions for trigonal symmetry are shown in Fig. 5. The transitions ${}^2E \rightarrow {}^2T_2$ were first observed by Klau-minzer, *et al.*⁴ Later Kushida² presented more complete data, but his linewidths at low temperature were instrument limited. Kushida also observed the ${}^2T_1 \rightarrow {}^2T_2$ transitions but was unable to separate components. In the spirit of the *R* and *B* lines which appear in the red and blue regions, respectively, these infrared transitions are designated the *I* lines. Individual transitions are identified by two subscripts for initial and final states which follow the numbers in parentheses in Fig. 5. For example, the transition from the lowest 2E level to the highest 2T_2 level is designated I_{13} .

Figure 6 shows the entire infrared spectrum at room temperature in both σ and π polarizations. This is very similar to Kushida's data. The arrows are the positions of the *I* lines predicted from the energies measured from the ground state.

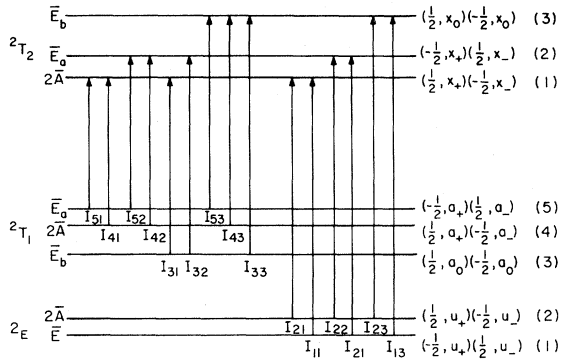


FIG. 5. Energy levels and transition notation for the I lines in ruby.

The allowed electric-dipole transitions are indicated.

At low temperature (Fig. 7) most of the $2E \rightarrow 2T_2$ transitions are completely separated. The measured positions, which shift with temperature, agree with ground-state measurement to within 0.1 cm^{-1} . The widths agree with the sum of the R - and B -line widths at various temperatures to within 2 cm^{-1} . Thus there is no doubt about the identity of these transitions.

The $2T_1 \rightarrow 2T_2$ absorption must be observed at temperatures where the $2T_1$ levels are appreciably populated. At room temperature, only about 6% of the excited ions are in the $2T_1$ states. From Fig. 6, it is clear that even with this low population, the measured absorption is comparable to the $2E \rightarrow 2T_2$ group. As the temperature is decreased, these lines are still not resolved, as expected from the R' linewidths (${}^4A_2 \rightarrow 2T_1$) which also remain broad. Figure 8 shows the $2T_1 \rightarrow 2T_2$ spectrum on an energy scale along with a trial-and-error component fit. Although such unfolding may appear unwarranted, only the intensities of the

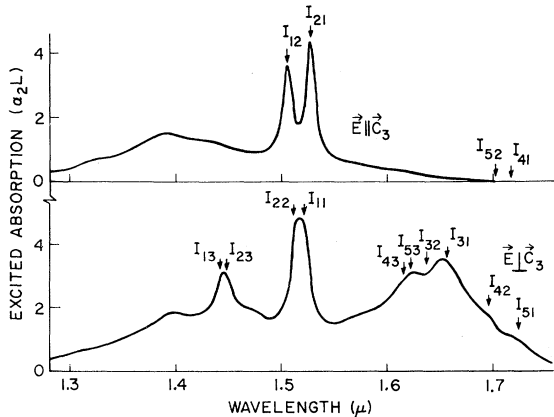


FIG. 6. Room-temperature infrared spectra of excited ruby (sample 1).

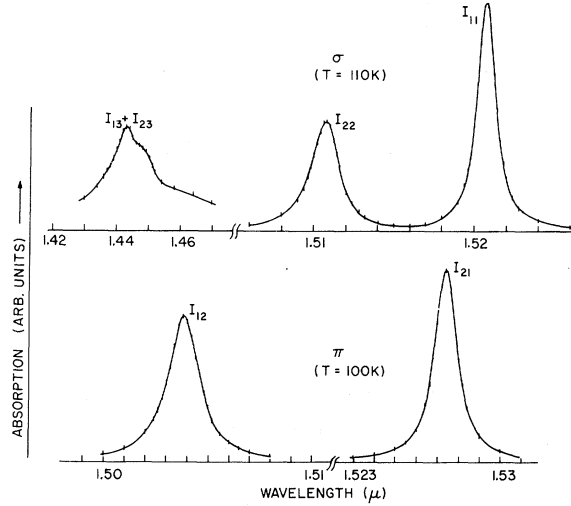


FIG. 7. $2E \rightarrow 2T_2$ spectra in ruby.

components were varied; the positions and widths were fixed by data for the R' and B lines. It should be noted that in fits at lower temperature each of the components decreased, following the Boltzmann distribution of the corresponding $2T_1$ sublevel. This confirms the identity of the transitions. The oscillator strength for the group is approximately 1.4×10^{-4} with a 20% uncertainty, or thirty times that measured for $2E \rightarrow 2T_2$. Table III gives the relative intensities of the I lines corrected for the Boltzmann distribution and normalized to the I_{11} line.

2. Emerald

The lowest excited-state levels in emerald are shown in Fig. 9. As expected from the compressive trigonal field, the levels are inverted with respect to ruby. The energies of the levels observed from the ground state are given; the dashed levels are uncertain for the $2T_1$ state²⁵ and are not ob-

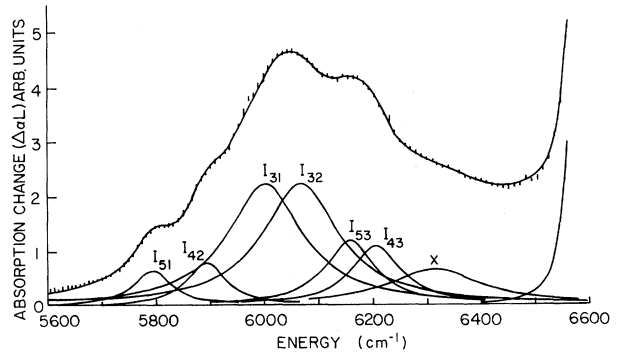


FIG. 8. Trial-and-error fit to the $2T_1 \rightarrow 2T_2$ absorption data in ruby at room temperature.

TABLE III. Relative intensities of the I lines normalized to the I_{11} line and corrected for the Boltzmann distribution.

	$j=1$	2	3
$i=1$	1.0	1.2	1.0
2	1.5	0.9	
3	30	30	~ 0
4	~ 0	15	30
5	15	~ 0	30

served at all for the 2T_2 state.¹³ The latter are probably broadened considerably by relaxation processes since the Debye temperature is much lower than in ruby while the splittings are larger.

The fluorescent lifetime of light emerald is much shorter than ruby,²⁵ ranging from 10^{-4} sec at room temperature to 10^{-3} sec at 77 K. The lifetime of our dark sample was observed to be reduced by nearly a factor of 2 from these values. To accommodate this shorter lifetime, the probelamp was pulsed at the time of maximum population as determined by the R -line fluorescent intensity. Since this time was during the pumping pulse, care was taken to avoid contamination of the probe signal by the pump.

The ${}^2E \rightarrow {}^2T_2$ absorption in σ polarization is shown in Fig. 10. A doublet occurs at precisely the energy difference expected from Fig. 9. As with the ruby results, the axial spectrum (light path along the optic axis) is identical to that shown, confirming the electric-dipole nature of the transition. No absorption was observed in π polarization. The integrated intensities of the lines are equal when corrected for the Boltzmann factor; the widths are 50 cm^{-1} for I_{33} and 48 cm^{-1} for I_{13} . The line designations are shown in Fig. 9. The subscripts are designated to agree with the ruby eigenfunction

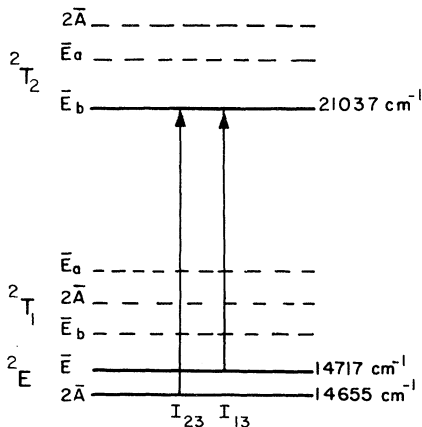


FIG. 9. Observed doublet levels in emerald (solid lines).

labels rather than the line positions.

The ${}^2T_1 \rightarrow {}^2T_2$ transitions are of interest for comparison with ruby where the corresponding absorption is very strong. The R' lines have not been firmly identified²⁵ so that an additional result would be locating the 2T_1 level. In order to balance the competing effects of Boltzmann factor and lifetimes (the former demands a high temperature, the latter a low temperature), a temperature was chosen where the product of the two is a maximum. No absorption was observed in the region $1.6\text{--}1.8 \mu\text{m}$. Given a minimum detectable absorption change and R' linewidths comparable to those found in ruby, the upper limit to the oscillator strength for the ${}^2T_1 \rightarrow {}^2T_2$ transition is established as $f \lesssim 2 \times 10^{-4}$. Thus the transition may indeed be strong but unobservable under present experimental conditions.

3. $\text{MgO}:\text{Cr}^{3+}$

The excited-state absorption in the region of the expected ${}^2E \rightarrow {}^2T_2$ transitions in $\text{MgO}:\text{Cr}^{3+}$ is shown in Fig. 11. For the single line observed at $1.550 \mu\text{m}$ (Fig. 12), the larger bands to shorter wavelengths appear very similar to the phonon sidebands of the R line. This line was first thought to be the magnetic dipole ${}^2E \rightarrow {}^2T_2$ (Γ_8) transition of the cubic system.²⁶ Refined population measurements, however, placed the oscillator strength at 3×10^{-7} if one assumes most of the chromium ions are in cubic sites. This is an order of magnitude greater than that predicted by Macfarlane, for the magnetic dipole transition.²⁷ Thus the previous assignment must be wrong.

Measurements of the B and R' ground-state transitions indicate that the observed transition is ${}^2E(\nu) \rightarrow {}^2T_2(\xi, \eta)$ of the chromium vacancy system. This assignment is corroborated by the position of the line, the intensity, and the electric dipole selection rules for the tetragonal perturbations. Under this assignment the oscillator strength is 3×10^{-6} if 10% of the ions are assumed to be in next-near-

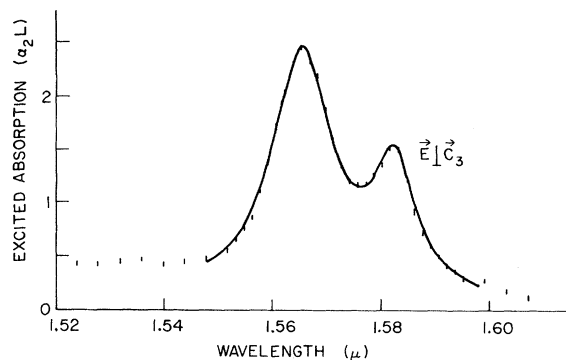


FIG. 10. ${}^2E \rightarrow {}^2T_2$ absorption in emerald at 97 K. The solid curve is a trial-and-error fit using two Lorentzians.

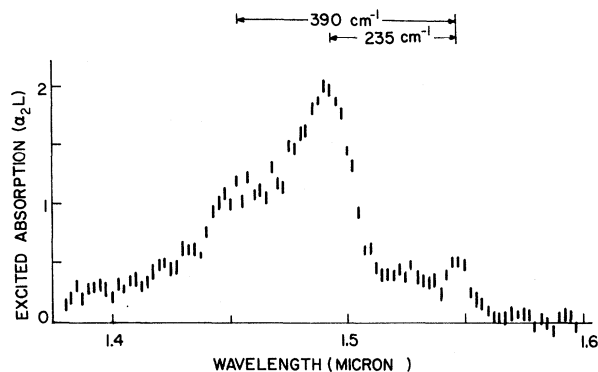


FIG. 11. Excited absorption spectrum of $\text{MgO}:\text{Cr}^{3+}$ (sample 1) at 160 K.

est-neighbor vacancy sites. It should be noted that absorption in the pair system also contributes to these lines. However, in this region the pair and vacancy lines are expected to be only slightly separated and not resolvable. No evidence of absorption in the I lines of the cubic system was observed.

B. Sharp line transitions to t_2^2e states

1. Ruby

Until recently, all spin-allowed transitions between the configurations t_2^3 and t_2^2e were observed as broad bands. This is to be expected because of the strong coupling between an e_g electron and the dominant cubic field. However, the sharp lines observed by Dunn and Francis indicate that cases of

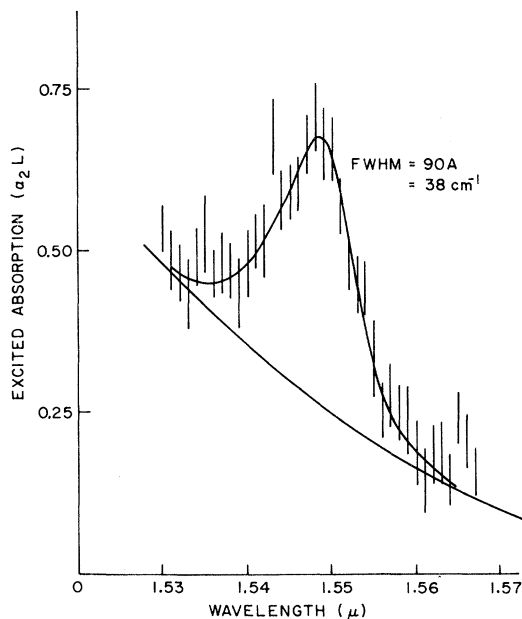


FIG. 12. I_1 line at 140 K in $\text{MgO}:\text{Cr}^{3+}$ (sample 1).

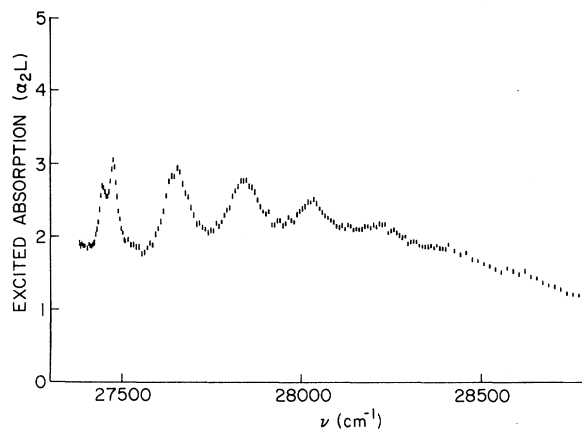


FIG. 13. ${}^2E \rightarrow {}^2A_2$ doublet and sidebands in ruby (sample 3) at 103 K.

weaker coupling do exist. Our measurements of the sharp excited-state transitions in the near uv and in the red are shown in detail in Figs. 13 and 14. The oscillator strength for the uv doublet is 2×10^{-6} . The phonon sideband series is quite clear and has a spacing of 190 cm^{-1} . The red doublet is much narrower and also much weaker with an oscillator strength of approximately 2×10^{-7} . The sidebands in this case appear very similar to the R line sidebands.

Dunn and Francis⁸ assigned these uv and red sharp lines to the ${}^2E \rightarrow {}^2A_2$ and ${}^2E \rightarrow {}^2A_1$ transitions by energy considerations. Further evidence supporting this assignment is given later in this paper.

The temperature dependence of the linewidth of these sharp doublets is shown in Fig. 15. Since both upper states 2A_1 and 2A_2 involve an e_g electron which might be more sensitive to crystal strains than a t_2 electron, one might expect a strain-limited linewidth at low temperatures larger

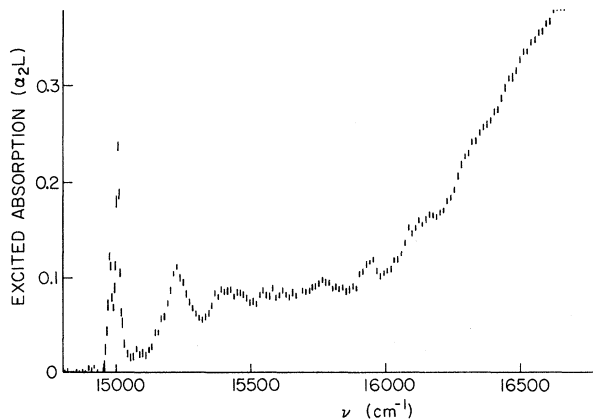


FIG. 14. ${}^2E \rightarrow {}^2A_1$ doublet and sidebands in ruby (sample 1) at 113 K.

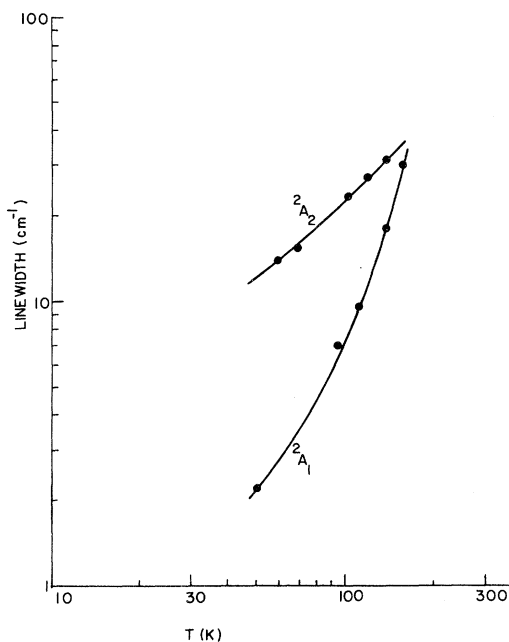


FIG. 15. Variation of the ${}^2E \rightarrow {}^2A_1$, 2A_2 linewidths in ruby with temperature.

than the $\sim 0.1 \text{ cm}^{-1}$ limit for the R lines. However, at our lowest temperature, 51 K, the ${}^2E \rightarrow {}^2A_1$ transition was pure Lorentzian within the limits of the data. With 20% as an upper limit for the inhomogeneous strain contribution, we get an upper limit of the strain width of the ${}^2E \rightarrow {}^2A_1$ transition of 0.4 cm^{-1} . This is only slightly greater than the strain limit of the R line.

2. Emerald

Having observed the ${}^2E \rightarrow {}^2A_2$ transition in ruby, we searched in detail the corresponding wavelength region in emerald. A broad bump similar to the sidebands of this transition in ruby was observed in σ polarization only. Apparently relaxation processes broaden the no-phonon transitions so that no sharp structure is resolved. The total oscillator strength of the ${}^2E \rightarrow {}^2A_2$ transition was 1×10^{-5} , which is somewhat weaker than in ruby.

3. $\text{MgO}:\text{Cr}^{3+}$

Sharp-line structure in the ${}^2E \rightarrow {}^2A_2$ transition was observed in $\text{MgO}:\text{Cr}^{3+}$. The region of the no-phonon lines in three samples varying from light yellow to dark green is shown in Fig. 16. There is only a single line in the light crystal, whereas more lines are evident in the darker crystals. A population ($\sim 4\%$) was determined only for sample 1 by doing a complete excited-state absorption spectrum. Thus absolute cross sections cannot be determined for the other samples. However, we can

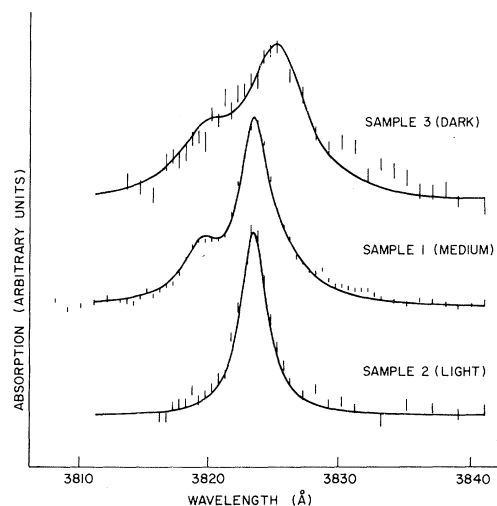


FIG. 16. The ${}^2E \rightarrow {}^2A_2$ transition no-phonon lines in three $\text{MgO}:\text{Cr}^{3+}$ samples.

estimate a population for these samples by assuming that the background absorption level (on the high-energy side of the ${}^2E \rightarrow c^2T_2$ band) is the same in all crystals. This is not unreasonable since the bands are probably predominantly vibronic and relatively independent of small crystal variations between the different types of sites. With this assumption, the parameters for the Lorentzians used to obtain the solid line fits in Fig. 16 are listed in Table IV.

Note that for comparison the peak absorptions are normalized to the Cr^{3+} density and length of sample 1.

The 3823.5-Å line, which is the only line appearing in the light sample, must be due to the cubic or vacancy system. We will see below that it must be of the vacancy system. At higher Cr^{3+} densities this line becomes weaker, presumably due to the capture of another Cr^{3+} ion on the opposite side of the vacancy. On the other hand, the line at 3825.3 Å increases approximately linearly with density until it dominates in the dark sample. One should not rely heavily on the listed intensities of this line since it was not resolved in sample 1, and part of its intensity quoted in sample 3 could come from the 3823.5 Å line. The 3819.5 Å line increases rapidly from sample 2 to sample 1 and

TABLE IV. Lorentzian linewidths (Å) and peak absorptions (cm^{-1}) (normalized to the Cr^{3+} density in sample 1) used to make the solid line fits in Fig. 15. The numbers in parentheses indicate possible contributions which were not included in the fits.

λ (Å)	ν (cm^{-1})	Sample 1	Sample 2	Sample 3
3819.5	26174.0	1.21	3.5 (< 0.4)	0.90
3823.5	26146.6	3.75	2.5	4.38
3825.3	26134.3	1.12	5.5 (< 0.4)	2.5
3830		(0.17)		3.675
				(0.4)

TABLE V. Lifetimes (in msec) of the R lines and the excited-state absorption (ESA) in the different systems of $\text{MgO}:\text{Cr}^{3+}$.

	Sample	λ (Å)	τ (R lines)	λ (Å)	τ (ESA)
Cubic	<i>a</i>	6981	10.1 ± 0.1		
	<i>b</i>	6891	$10.5^a \pm 0.1$		
	<i>c</i>	6981	8.5 ± 0.1		
Vacancy $E(u)$	<i>a</i>	6992			
	<i>b</i>	6992	6.0 ± 0.1		
	<i>c</i>	6992	5.5 ± 0.1		
$E(v)$	<i>a</i>	7038	6.9 ± 0.1	3823.5	7.1 ± 0.5
	<i>b</i>	7038	6.3 ± 0.1	3823.5	6.7 ± 0.3
	<i>c</i>	7038	5.30 ± 0.05		
pair and vacancy $E(u)$	<i>a</i>		...		
	<i>b</i>		...		
	<i>c</i>	6989	7.7 ± 0.4		
$E(v)$	<i>a</i>				
	<i>b</i>	7034	6.50 ± 0.05	3819.5	7.0 ± 1.0
	<i>c</i>	7034	5.60 ± 0.06		

^aHigher than *a* due to self-trapping?

appears to be slightly smaller in sample 3. However, the latter number has a large uncertainty because the data are not as good as for the other samples. Either of these lines, or both, could be associated with pair system transitions. There also appears to be a small amount of absorption around 3830 Å which increases linearly with density. This could be associated with the unidentified satellite lines observed in ESR and in ground-state absorption around 7000 Å.

To confirm the assignments the lifetimes of the various types of 2E sites were measured under flashlamp excitation. The lifetime of the excited absorption in the different lines was also measured by varying the time delay between pump and probe pulses. While some energy transfer is known to occur from cubic to noncubic sites,²⁸ this did not appreciably affect our results since the fluorescence and excited absorption were measured under identical conditions. Resonant absorption and re-emission is likewise a small effect.

The results of a weighted least-squares fit to the exponential decay are listed in Table V. The cubic site is clearly ruled out for the 3823.5- and 3819.5-Å lines. The error for the 3819.5-Å line is large, but the results are consistent the above pair system assignment. No lifetime measurements were made on the 3825.3-Å line since it was not resolved from the 3823.5-Å line.

C. Broad band transitions to t_{2g}^2e states

The oscillator strengths of the ground- and excited-state absorption bands in Table II were determined from the peak absorption and width of the bands. Actual integration would produce slightly

more accurate results. Note that the excited-state bands are of similar strength to the ground-state bands and are of comparable strength in all three crystals.

III. THEORETICAL

A. Energy level calculations

There are two basic approaches to energy level calculations of transition-metal ions in a crystal lattice: one begins with either strong- or weak-field basis functions. The strong-field approach has the advantage of being able to identify levels with certain symmetries of the crystal field. Selection rules can often be obtained from group-theoretical arguments. However, because the crystal field is actually of only intermediate strength, considerable mixing of strong-field states occurs. First- and second-order perturbation theory is not always useful.²⁹ In the weak-field approach it is more difficult to assign symmetries to the eigenvalues. However, this method allows corrections to the free ion energies such as a Trees correction³⁰ to be incorporated into the calculation. If one cannot calculate the free ion levels accurately,³¹ one will probably not be able to calculate the impurity ion levels accurately.

In our calculations we have used both methods; the choice was made on the availability of matrices already tabulated. The strong-field matrices of Eisenstein³² were used to calculate the cubic field plus spin-orbit interaction case. The weak-field matrices of Macfarlane³³ and Jesson³⁴ were used to incorporate trigonal and tetragonal fields, respectively. The Trees correction was simply incorporated by adding a $\alpha L(L+1)$ term to the diagonal

TABLE VI. Calculated and observed energy levels for ruby and emerald. All numbers are in cm^{-1} .

	Ruby		Emerald	
	Calc.	Obs.	Calc.	Obs.
$a^2E (t_2^3)$	14 171	14 418 14 447	14 472	14 655 14 717
$a^2T_1 (t_2^3)$	14 744 14 875	14 957 15 168	14 944 15 347	
${}^4T_2 [t_2^2 ({}^6T_1)e]$	18 002 18 453	18 000 σ 18 400 π	16 043 16 727	15 700 π 16 800 σ
$a^2T_2 (t_2^3)$	21 308 21 687	20 993 21 068 21 357	21 085 22 262	21 037
$a^4T_1 [t_2^3 ({}^6T_1)e]$	24 079 25 158	24 300 σ 25 100 π	22 855 23 759	22 800 σ 24 000 π
${}^2A_1 [t_2^2 ({}^4E)e]$	30 308	29 425	28 758	
$b^2T_2 [t_2^2 ({}^6T_1)e]$	32 312 32 753	32 500 π 32 550 σ	30 666 30 786	30 700 π 31 650 σ
$c^2T_1 [t_2^2 ({}^4T_2)e]$	32 622 32 915		31 644 32 036	
$b^2E [t_2^2 ({}^4E)e]$	34 329		33 215	
$b^2T_1 [t_2^2 ({}^6T_1)e]$	37 034 37 523	36 700 π 37 100 σ	36 126 36 138	36 300 σ $\sim 37 400 \pi$
$b^4T_1 [t_2e^2 ({}^6A_2)]$	39 069 39 176	39 000 σ 39 000 π	34 319 37 479	
$c^2T_2 [t_2^2 ({}^4T_2)e]$	40 792 41 297	41 100 σ 41 100 π	40 518 40 752	39 900 σ $\sim 39 900 \pi$
${}^2A_2 [t_2^2 ({}^4E)e]$	42 678	41 894	42 241	41 800
Dq	1815		1640	
B	645		710	
C	3000		2960	
ν	800		-1550	
ν'	680		1380	
α	70		70	

matrix elements. (L is the orbital angular momentum of the free ion basis state.) Our minicomputer was not large enough to diagonalize the complete matrices of Macfarlane which incorporated cubic and trigonal fields plus the spin-orbit interaction. Since trigonal field splittings generally dominate over spin-orbit splittings, we chose to diagonalize the simpler set of cubic-plus-trigonal-field matrices. For the tetragonal-field case the complete matrix was diagonalized on a large computer.

For ruby and emerald which have trigonal fields, the weak-field matrices were used. It was found that a Trees correction (we used the free ion value, $\alpha = 70 \text{ cm}^{-1}$) definitely improves the fit of the theoretical levels to the experimental results. In particular it improves the agreement of the $(t_2^3)^2T_2$ level which has been hard to fit in the past without this correction.³³ The best-fit energy levels are listed in Table VI and indicated in Figs. 2 and 3.

For the cubic system in $\text{MgO}:\text{Cr}^{3+}$ the strong-field matrices were used. The weak-field matrices were also tried to check the effect of a Trees correction. The two fits produced comparable results.

For the noncubic systems, the weak-field matrices were used. The results for all systems are tabulated in a previous paper.³⁵

One should note in evaluating the fit of energy-level calculations to experiment that one ordinarily relies heavily on the positions of the peaks of the ground-state absorption bands to determine the cubic field parameters B and C . This is because states of t_2^2e configuration are much more sensitive to these parameters than t_2^3 states. Unfortunately, the matrices used above do not incorporate the electron-phonon interaction, which plays a major role in determining the shape and position of a band. Therefore one may derive incorrect parameters by assuming that the peak of the band coincides with the pure electronic level calculated from the matrices. However, we will see that this assumption is approximately correct.

When interactions of the impurity ion electron with the lattice are included with the normal parabolic harmonic oscillator potential curve, an additional term, linear in the normal-mode coordinates q_j , is added³⁶:

$$\Delta E_\alpha = N^{-1/2} \sum_j A_j^\alpha q_j. \quad (8)$$

The coefficients A_j^α depend on the electron-lattice interaction in the state α . For a nondegenerate state these coefficients are small.³⁶ For degenerate states, however, the potential curve will be shifted in q_j space. The intercept of the curve with the $q_j = 0$ axis will remain the same, but the potential minimum will be lower and will occur off the axis. This is the well-known Jahn-Teller theorem.

The shape of transitions between two states will depend on the relative shifts of the potential curves. If the two states are not shifted, the sharp no-phonon line will predominate. If one state has a large shift, absorption will occur from the zero- or one-phonon level s of the lower state a to multiphonon levels of the upper state b . Thus the absorption will be broadened into a band. Using the semiclassical Franck-Condon approximation, Lax shows that the mean absorption energy is³⁷

$$\hbar\bar{\nu} = E_b - E_a - \langle (A_j^b - A_j^a)A_j^a / (M\omega_j^2) \rangle. \quad (9)$$

Note that if state a has little or no electron-lattice interaction ($A_j^a \sim 0$), then the mean absorption energy coincides with the separation of the pure electronic states, $E_b - E_a$. This certainly applies to transitions from the nondegenerate 4A_2 state. It is also true for transitions from other metastable t_2^3 states, 2E and 2T_1 . This is because a first-order Jahn-Teller distortion does not occur for the half-filled configuration, t_2^3 .³⁶

There are many assumptions made in this simple argument, including the neglect of mixing of electronic states by nuclear motion. One should therefore expect errors of 10% to 20% of the zero

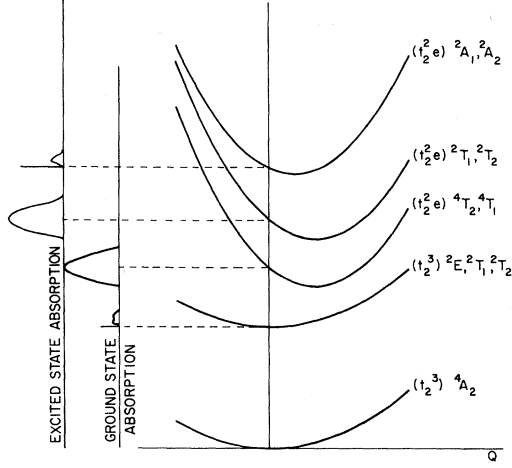


FIG. 17. Pictorial representation of the potential curves for the states of Cr^{3+} in an octahedral lattice. The coordinate Q is representative of displacement in one of several symmetry coordinates of the lattice.

phonon line shift in the determination of $E_b - E_a$ from the band peaks. The fact that bands and lines can be fit with the same parameters to within a few hundred wave numbers when the zero phonon line shift of the bands is about 1500 cm^{-1} indicates that the above approximations are not unreasonable.

The expected types of potential curves for the

different states involved in this analysis are shown in Fig. 17. The position coordinate Q represents displacement in one of several possible symmetry coordinates. One can see why the observed ground- and excited-state transitions are bands or sharp lines from this diagram.

B. Transition probabilities: Lines

In this section we will determine selection rules and intensities for electric-dipole transitions slightly allowed by a weak odd-parity crystal field. The predictions will be compared to the experimental data for the sharp lines observed in excited-state absorption given above. In this way the transition assignments can be confirmed.

For the electric-dipole transitions we use the technique of closure, as developed by Shinada, Sugano, and Kushida.⁵ This elegant method greatly simplifies the calculations by summing over the many odd-parity intermediate states. The approximations required in order to invoke closure can be quite severe, however, so that it must be used with caution. The more tedious method of specifying in detail all of the odd parity states, as applied to the t_2^3 transitions in ruby, has also been employed elsewhere.²⁶

As is well known, under perturbation theory the electric-dipole matrix element for a normally parity-forbidden transition slightly allowed by an odd-parity field V^{odd} is

$$\begin{aligned} \langle \alpha S \Gamma \gamma M_s | \vec{P} | \alpha' S' \Gamma' \gamma' M_s \rangle &= \sum_{\alpha'', \Gamma'' \gamma'' M_s, i} \frac{\langle \alpha S \Gamma \gamma M_s | \vec{P} | \alpha'' S \Gamma'' \gamma'' M_s \rangle \langle \alpha'' S \Gamma'' \gamma'' M_s | V_i^{\text{odd}} | \alpha' S' \Gamma' \gamma' M_s \rangle}{W(\alpha' S' \Gamma' \gamma' M_s) - W(\alpha'' S \Gamma'' \gamma'' M_s)} \\ &\times \sum_{\alpha''', \Gamma''' \gamma''' M_s, i} \frac{\langle \alpha S \Gamma \gamma M_s | V_i^{\text{odd}} | \alpha''' S \Gamma''' \gamma''' M_s \rangle \langle \alpha''' S \Gamma''' \gamma''' M_s | \vec{P} | \alpha' S' \Gamma' \gamma' M_s \rangle}{W(\alpha S \Gamma \gamma M_s) - W(\alpha''' S \Gamma''' \gamma''' M_s)}, \end{aligned} \quad (10)$$

where α is the electronic configuration, and γ is the component of state Γ . Since we are dealing with spin-allowed transitions, S and M_s must remain constant throughout and will be dropped to simplify notation. Under closure the two sums are combined, and

$$\begin{aligned} \langle \alpha \Gamma \gamma | P_k | \alpha' \Gamma' \gamma' \rangle &= \sum_i \frac{2}{\Delta W} \langle \alpha \Gamma \gamma | P_k V_i^{\text{odd}} | \alpha' \Gamma' \gamma' \rangle, \end{aligned} \quad (11)$$

where ΔW is a "suitable average of energies," and P_k is the k th component of $\vec{P} = \sum_i e \vec{r}_i$ which transforms as T_{1u} under a cubic field. $P_k V_i^{\text{odd}}$ can be expressed as

$$\begin{aligned} P_k(T_{1u}) V_i^{\text{odd}}(\Gamma_{ui} 0) &= \sum_{\bar{\Gamma} \bar{\gamma}} X_{\bar{\gamma}}(\bar{\Gamma} : \Gamma_{ui}) \langle \bar{\Gamma} \bar{\gamma} | T_{1u} k, \Gamma_{ui} 0 \rangle. \end{aligned} \quad (12)$$

In practice this simply tells us which $\bar{\Gamma} \bar{\gamma}$ to use in the matrix element in Eq. (11). Applying the Wigner-Eckart theorem, the final result is

$$\begin{aligned} \langle \alpha \Gamma \gamma | P_k | \alpha' \Gamma' \gamma' \rangle &= \sum_i \frac{2}{\Delta W} \sum_{\bar{\Gamma} \bar{\gamma}} \langle \bar{\Gamma} \bar{\gamma} | T_{1u} k, \Gamma_{ui} 0 \rangle \\ &\times \langle \alpha \Gamma \gamma | \Gamma' \gamma', \bar{\Gamma} \bar{\gamma} \rangle \langle \alpha \Gamma \| \bar{X}(\bar{\Gamma} : \Gamma_{ui}) \| \alpha' \Gamma' \rangle, \end{aligned} \quad (13)$$

where the reduced matrix elements are those for three electrons.

The analysis which follows will again be divided into two sections according to the configuration of the terminal state of the transition. We will show that the polarization of the observed transitions agree with the closure predictions. However, the intensities of some transitions cannot be explained under this crystal field treatment without a more

TABLE VII. Identification of the 2E , ${}^2T_1 \rightarrow {}^2T_2$ I -line transitions.

i	I_{ij}			
	$j=1$	2	3	
1	σ_1	π_1	σ_2	\bar{E}
2	π_1	σ_1	σ_2	$2\bar{A}$
3	σ_5	σ_5	π_3	\bar{E}_b
4	π_2	σ_3	σ_4	$2\bar{A}$
5	σ_3	σ_4	σ_4	\bar{E}_a
	$2\bar{A}$	\bar{E}_a	\bar{E}_b	

2T_2

detailed understanding of the chromium environment.

C. Transitions to $(t_2^3) {}^2T_2$

1. Ruby

Of the three odd-parity fields in ruby— $V_1(T_{1u}a_0)$, $V_2(T_{2u}\chi_0)$, and $V_3(A_{2u}e_2) - V_1(T_{1u}a_0)$ is expected to have the largest contribution to most transitions since it appears in first order in the power series expansion with respect to the electron coordinate r . The other two terms do not appear until third order. Thus it is usually assumed that $V_1(T_{1u}a_0)$ dominates.^{5,38,39}

Shinada, Sugano, and Kushida have calculated the intensities for the transitions considered here.⁵ Their results are shown in Tables VII and VIII. Within experimental error (which is small for the narrow ${}^2E \rightarrow {}^2T_2$ lines) the observed transitions accurately follow the predicted polarization. An immediate conclusion can be drawn from this: the mixing of \bar{E}_a and \bar{E}_b components of 2T_2 must be negligible.

The experimental intensities in Table III can be approximately described by the following choice of parameters:

$$2\sigma_3 = \sigma_4 = \sigma_5 = 30\sigma_1,$$

$$\pi_1 = 1.4\sigma_1 = 2.8\sigma_2,$$

$$\pi_2 = \pi_3 \sim 0.$$

If $V_1(T_{1u})$ is assumed to be the dominant odd-field term, then an intensity ratio $\pi_1/\sigma_1 = 4$ is predicted. The observed ratio $\pi_1/\sigma_1 = 1.4$ is a radical departure from this prediction. This indicates that the first-order $V_1(T_{1u})$ terms must be reduced in this case to the same strength as the third-order terms $V_2(T_{2u})$ and $V_3(A_{2u})$. The reason for this reduced influence is that both the initial and final states of the transition are of configuration t_2^3 . The I transitions involve only t_{2g} electrons which are not per-

turbed as strongly by a T_{1u} field as e_g electrons. One might have expected this effect to have been seen before in other transitions within t_2^3 : the R , R' , and B lines. These transitions, however, actually involve an e_g electron since they occur through spin-orbit coupling to the $(t_2^2 e) {}^4T_2$ and 4T_1 bands. The complications of phonon-assisted transitions prevent determination of the pure electronic contribution in these bands. One can expect from the above arguments, however, that the electronic contribution to the ground- and excited-state bands would be stronger than the integrated I -line intensity.

The most unexpected feature of the I -line spectra is the σ -polarized strengths of the ${}^2T_1 \rightarrow {}^2T_2$ transitions which are fifteen and thirty times the strength of the ${}^2E \rightarrow {}^2T_2$ transitions. From Table VIII only the terms $B(V_1)$ and $B(V_2)$ can account for this result.^{5,40} That is, the $B(V_i)$ terms must be an order of magnitude larger than the $A(V_i)$ terms. Unfortunately no choice of A and B parameters can account for the factor of 2 difference between σ_3

TABLE VIII. Transition intensities of the I lines using closure.

$\pi_1 = \frac{4}{9\Delta W^2} [2A(V_1) - \sqrt{6} A(V_3)]^2$
$\sigma_1 = \frac{4}{9\Delta W^2} \{ [A(V_1) + \sqrt{6} A(V_3)]^2 + 3A(V_2)^2 \}$
$\sigma_2 = \sigma_1$
$\pi_2 = \frac{2}{9\Delta W^2} [2A(V_1) - \sqrt{6} A(V_3)]^2$
$\sigma_3 = \frac{12}{9\Delta W^2} [B(V_1)^2 + B(V_2)^2]$
$\sigma_4 = \frac{2}{9\Delta W^2} \{ [A(V_1) - \sqrt{6} B(V_1) + \sqrt{6} A(V_3)]^2 + 3[A(V_2) + \sqrt{2} B(V_2)]^2 \}$
$\sigma_5 = \frac{2}{9\Delta W^2} \{ [A(V_1) + \sqrt{6} B(V_1) + \sqrt{6} A(V_3)]^2 + 3[A(V_2) - \sqrt{2} B(V_2)]^2 \}$
$\pi_3 = 0$

where

$$A(V_i) = \langle t_{2g} \| X(T_{2g} : \Gamma_{ui}) \| t_{2g} \rangle$$

$$= \frac{1}{\sqrt{2}} \langle t_{2g}^3 {}^2E_g \| X(T_{2g} : \Gamma_{ui}) \| t_{2g}^3 {}^2T_{2g} \rangle$$

$$= - \langle t_{2g}^3 {}^2T_{1g} \| X(T_{2g} : \Gamma_{ui}) \| t_{2g}^3 {}^2T_{2g} \rangle$$

$$B(V_i) = \langle t_{2g} \| X(E_g : \Gamma_{ui}) \| t_{2g} \rangle$$

$$= \frac{1}{\sqrt{3}} \langle t_{2g}^3 {}^2T_{1g} \| X(E_g : \Gamma_{ui}) \| t_{2g}^3 {}^2T_{2g} \rangle$$

and both σ_4 and σ_5 . Nor can this theory account for σ_1 and σ_2 , which are equal in theory but differ by a factor of 2 experimentally. The vanishing of π_2 indicates that $V_2(T_{2u})$ may be the dominant term in the ${}^2E \rightarrow {}^2T_2$ transitions, but again there is a discrepancy since one would have expected $\pi_2 = \frac{1}{2}\pi_1$ from Table VIII.

One can conclude, therefore, that the closure theory explains the general features of the I lines in ruby. The correct lines are predicted in the proper polarization. However, there are discrepancies of up to factors of 2 in some of the relative intensities.

2. Emerald

The analysis is the same for emerald as for ruby except only the T_{2u} terms are used. The observed ${}^2E \rightarrow {}^2T_2$ transitions correspond to σ_2 terms in Table VIII, where

$$\sigma_2 = [4/3(\Delta W)^2][A(V_2)]^2. \quad (14)$$

There is no absorption in π polarization, as expected. The large oscillator strength, $f \approx 4 \times 10^{-6}$ (comparable to ruby) indicates that a T_{2u} crystal field can produce moderately strong transitions within the f^2 configuration. This supports our assumption that the $A(V_2)$ term is dominant in the ${}^2E \rightarrow {}^2T_2$ transitions in ruby. The experimental upper limit of the oscillator strength of the ${}^2T_1 \rightarrow {}^2T_2$ transitions, $f \lesssim 2 \times 10^{-4}$ does not answer the question of whether or not a T_{2u} field causes enhancement of these lines relative to the ${}^2E \rightarrow {}^2T_2$ transitions.

3. MgO:Cr³⁺

As stated previously the predicted magnetic dipole transitions in the cubic system are not strong enough to account for the one I line observed at $1.550 \mu\text{m}$ in MgO:Cr³⁺. Thus we need to consider electronic dipole transitions which are slightly allowed in the vacancy and pair system. The tetragonal odd-parity fields are of type $T_{1u}\gamma$ and $E_u\mu$.⁴¹ T_{1u} enters in first order in the power-series expansion, whereas E_u does not enter until fifth order. Thus we can expect $V(T_{1u}\gamma)$ to be the dominant term.

Since $E \times T_2 = T_1 + T_2$, the only possible closure operators are $\bar{\Gamma} = T_{1u}$ and T_{2g} in Eq. (12). The relation⁹

$$\langle t_2^3 {}^2E \parallel \bar{X}(T_{1g}) : \Gamma_{u1} \parallel t_2^3 {}^2T_2 \rangle \\ \propto \langle t_{1g} \parallel X(T_{1g} : \Gamma_{u1}) \parallel t_{2g} \rangle = 0, \quad (15)$$

leaves only one operator $\bar{\Gamma} = T_{2g}$. This greatly simplifies the results which appear in Table IX. That only one line is observed is understandable. First, the ξ and η components of 2T_2 are not split by a tetragonal field. Only spin-orbit coupling can cause a small splitting between two linear combinations

of these states, and the splitting is calculated to be only 1 cm^{-1} in this case.³⁵ This is much smaller than the linewidth of 38 cm^{-1} . Second, the unobserved ${}^2E(u) \rightarrow {}^2T_2(\xi, \eta)$ transitions should be reduced in intensity by a factor of 3 times the Boltzmann factor 1.46, or a factor of 4.4 from the observed line. The experimental sensitivity was only a factor of 3 lower than the observed line, so the nonobservation of the ${}^2E(u) \rightarrow {}^2T_2(\xi, \eta)$ transition is in agreement with theory. Unfortunately, line broadening and phonon-assisted sidebands prevented observation at high temperatures where the Boltzmann factor is more favorable.

D. Transitions to $t_2^3 e$: Bands

1. Ruby and emerald

The excited-state bands should occur with a large strength from both the 2E and 2T_1 levels. However, since the most of the excited population is in the 2E level, we can assume for a theoretical analysis that most of the observed band absorption comes from the 2E level.

Using the closure approximation, Shinada, Sugano, and Kushida have calculated the intensities of the four ${}^2E \rightarrow b, c^2T_1; b, c^2T_2$ bands⁵:

$$\begin{aligned} \sigma_{1,2}^{\pm} &= \frac{2}{9\Delta W^2} [3D(T_{1u})^2 + D(T_{2u})^2], \\ \pi_{1,2} &= \frac{16}{9\Delta W} D(T_{2u})^2, \\ \sigma_{3,4}^{\pm} &= \frac{2}{9\Delta W^2} \{ [C(T_{1u}) + \sqrt{6}C(A_{2u})]^2 + 3C(T_{2u})^2 \}, \\ \pi_{3,4} &= \frac{8}{9\Delta W^2} [\sqrt{2}C(T_{1u}) - \sqrt{3}C(A_{2u})]^2. \end{aligned} \quad (16)$$

The subscripts 1, 2, 3, 4 refer to transitions to the $b^2T_2, c^2T_1, b^2T_1,$ and c^2T_2 states, respectively. Since there are transitions to two substates in σ polarization and to one substate in π polarization in each case, we must multiply the σ_i 's by two when comparing to experimental results in Table II.

The first two bands are not resolved experimentally. Thus the $\sigma_1 = \sigma_2$ and $\pi_1 = \pi_2$ relations cannot be tested. In ruby the band in σ -polarization is stronger, indicating that the T_{1u} field (or T_{1u} vibrations) makes the predominant contribution. How-

TABLE IX. Predicted electric-dipole intensities for the vacancy system ${}^2E \rightarrow {}^2T_2$ transitions [in units of $A^2/3\Delta W^2$, where $A = \langle t_{2g} \parallel T_{2g} : T_{1u} \parallel t_{2g} \rangle$.]

		2T_2		
		ξ	η	ζ
2E	u	1	1	0
	v	3	3	0

ever, the large absorption in π indicates that T_{2u} contributions are nearly as important. In emerald the π absorption is stronger, indicating that T_{2u} dominates. Some T_{1u} contribution is needed, however, to explain the observed $\pi/\sigma \sim 2$ ratio. The above observations are in general agreement with the expected T_{1u} and T_{2u} static fields in ruby and emerald, respectively. However, one cannot rule out T_{1u} and T_{2u} odd vibrations as the source of the absorption strength rather than the static field. In fact, the T_{1u} contribution in emerald can come only from odd vibrations: Bands 3 and 4 are predicted to be equal in both polarizations but differ by 30% experimentally in ruby. The extra strength of band 4 could be due to a smaller energy dominator since the c^2T_2 state is closer to the odd-parity states. One could use this information to place the odd parity states at around $80\,000\text{ cm}^{-1}$ from the ground state. However, in view of larger discrepancies in calculating the dichroic nature of the ground-state bands,³⁸ this prediction cannot be taken very seriously. In emerald, band 4 is also slightly larger in both polarizations, but bands 3 and 4 are only barely resolved, and accurate oscillator strengths cannot be determined.

The observed dichroic ratios for bands 3 and 4 favor a predominant T_{1u} field in ruby and T_{2u} field in emerald, although large contributions from the other fields are also needed. This is in agreement with the analysis of bands 1 and 2.

2. MgO:Cr³⁺

Using the closure approximation [Eq. (13)] we have calculated the intensities of the excited-state bands in a cubic basis with T_{1u} and E_u tetragonal perturbing fields. The results are shown in Table X. Unfortunately, since the tetragonal symmetry axes in MgO:Cr³⁺ are randomly distributed, the interesting selection rules in Table X cannot be tested. Perhaps with polarized excitation of the 2E excited state, experiments to test these selec-

TABLE X. Transitions in a cubic basis allowed by T_{1u} ξ and E_u u tetragonal fields. The parameters are the following: $\sigma_{1,2} = (1/3\Delta W^2)[D(T_{1u})^2 + \frac{1}{2}D(E_u)^2]$; $\pi_{1,2} = (8/3\Delta W^2)D(E_u)^2$; $\sigma_{3,4} = (1/3\Delta W^2)[C(T_{1u})^2 + \frac{3}{2}C(E_u)^2]$.

		2E	
		u	v
c^2T_1	α, β	σ_1	$3\sigma_1$
	γ	0	π_1
b^2T_2	ξ, η	$3\sigma_2$	σ_2
	ξ	0	π_2
b^2T_1	α, β	$3\sigma_3$	σ_3
	γ	0	0
c^2T_2	ξ, η	σ_4	$3\sigma_4$
	ξ	0	0

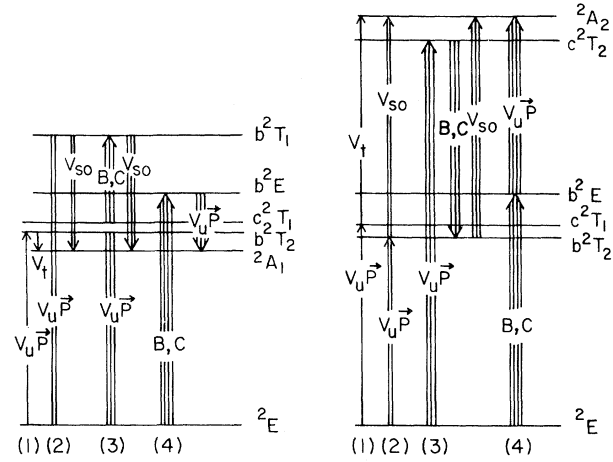


FIG. 18. Possible sources for the observed strength of the ${}^2E \rightarrow {}^2A_1, {}^2A_2$ transitions.

tion rules will be done in the future. The present experiment can only test the predicted equality of bands 3 and 4 (bands 1 and 2 are not resolved in this case either).

From Table II the bands are seen to be about equal but with band 3 (${}^2E \rightarrow b^2T_1$) slightly larger. This is the opposite of ruby and emerald. This casts doubt on the validity of making conjectures on the position of the odd parity levels from slight band intensity differences.

E. Transitions to t_2^2e : Lines

1. Ruby and emerald

If one tries to apply Eq. (13) to the ${}^2E \rightarrow {}^2A_1, {}^2A_2$ transitions, one finds that the reduced matrices $\langle \alpha\Gamma || \bar{X}(\bar{\Gamma} : \Gamma_{ui}) || \alpha'\Gamma' \rangle$ vanish. This is because the 2A_1 and 2A_2 states lack a common t_2^2 parent with the metastable 2E state. Thus it is surprising that one sees such strong absorption in these transitions since they are forbidden even via odd-parity perturbations.

To explain the experimental results one looks for configuration mixing in the initial and final states. The transitions might borrow intensity from a nearby strong band via trigonal field or spin-orbit coupling (terms 1 and 2 in Fig. 18) as the R and B lines borrow from the ground-state bands. To make the energy denominators more favorable, the states may borrow from the small Coulomb admixture of another state in a nearby band (term 3). Or the transitions might borrow intensity by direct Coulomb admixture (term 4) in analogy to the ${}^4A_2 \rightarrow b^4T_1$ band.

The contribution of these terms to the observed oscillator strength in ruby is shown in Table XI. The numbers would be quite similar for emerald. The trigonal field contributions (term 1) give the right polarization but are too small to account for

TABLE XI. Contributions to the ${}^2E \rightarrow {}^2A_1$, 2A_2 oscillator strengths in units of 10^{-6} from the mixing terms shown in Fig. 18.

		(1)	(2)	(3)	(4)	Obs.
${}^2E \rightarrow {}^2A_1$	σ	0.41	0.006	0.004	~ 1	1.5
	π	0	0.004	0.003	0	
${}^2E \rightarrow {}^2A_2$	σ	0.04	0.001	0.05 ^a	~ 1	50
	π	0	0.001	0.07 ^a	0	

^aCalculated using $\Delta E = 700 \text{ cm}^{-1}$.

the large ${}^2E \rightarrow {}^2A_2$ strength. Spin-orbit terms give the wrong polarization and are negligible except for term 3 in the ${}^2E \rightarrow {}^2A_2$ transition. This is an interesting case because the 2A_2 level sits on the side of the $c {}^2T_2$ band. Thus the energy denominator is uncertain. The 700 cm^{-1} splitting between the 2A_2 no-phonon line and the $c {}^2T_2$ band peak was used for the calculation. However, if the vibronic overlap with $c {}^2T_2$ multiphonon levels near the 2A_2 level were large, the energy denominator might be much smaller. To fit the observed 5×10^{-5} oscillator strength in σ , however, an effective energy denominator of 20 cm^{-1} is needed. Denominators this small may be possible, but then a stronger absorption in π would also be predicted. Since no absorption is seen in π , the contribution from term 3 must be small.

Term 4 is the most probable source of the ${}^2E \rightarrow {}^2A_1$, 2A_2 intensities. This term arises from a 9.4% admixture of the $b {}^2E$ state, which has a common parent with the 2A_1 and 2A_2 states, into the metastable $a {}^2E$ level. The transition can now occur via the closure theory, but will be reduced by $(0.094)^2 \sim 10^{-2}$. If one assumes that the $b {}^2E \rightarrow {}^2A_1$, 2A_2 strength is similar to other ground- and excited-state bands ($f \sim 10^{-4}$) then one can explain the ${}^2E \rightarrow {}^2A_1$ strength but not the ${}^2E \rightarrow {}^2A_2$ strength. The details of the closure theory follow.

For ${}^2E \rightarrow {}^2A_1$, 2A_2 transitions the only closure operators which give nonzero $\langle \Gamma\gamma | \Gamma'\gamma', \bar{\Gamma}\bar{\gamma} \rangle$ in Eq. (13) are $\bar{\Gamma}\bar{\gamma} = {}^2Eu_{\pm}$ for transitions from the ${}^2Eu_{\pm}$ state. The $\langle \bar{\Gamma}\bar{\gamma} | T_{1u}k, \Gamma_{ui}0 \rangle$ coefficient can then be calculated to predict equal transitions in σ polarization only from both 2E levels with $V(T_{1u}a_0)$ or $V_2(T_{2u}\chi_0)$. $V_3(A_{2u}e_2)$ cannot induce these transitions. Numerically the transition strengths from $b {}^2Eu_{\pm}$ to 2A_1 or 2A_2 via $k = \pm 1$ can be written

$$\begin{aligned} \sigma^{\pm}({}^2A_1) &= \frac{8}{9\Delta W^2} \{ [E(T_{1u}) + (\frac{1}{2}\sqrt{3})F(T_{1u})]^2 \\ &\quad + [E(T_{2u}) + (\frac{1}{2}\sqrt{3})F(T_{2u})]^2 \}, \\ \sigma^{\pm}({}^2A_2) &= \frac{8}{9\Delta W^2} \{ [E(T_{1u}) - (\frac{1}{2}\sqrt{3})F(T_{1u})]^2 \\ &\quad + [E(T_{2u}) - (\frac{1}{2}\sqrt{3})F(T_{2u})]^2 \}, \end{aligned} \quad (17)$$

where $E(\Gamma_{ui})$ and $F(\Gamma_{ui})$ are the single-electron reduced matrix elements

$$\begin{aligned} E(\Gamma_{ui}) &\equiv \langle t_2 \| x(E; \Gamma_{ui}) \| t_2 \rangle, \\ F(\Gamma_{ui}) &\equiv \langle e \| x(E; \Gamma_{ui}) \| e \rangle. \end{aligned} \quad (18)$$

The $E(\Gamma_{ui})$ are identical to the $B(\Gamma_{ui})$ parameters which were found to be the major contributors to the strong ${}^2T_1 \rightarrow {}^2T_2$ I lines. Thus the $E(\Gamma_{ui})$ should cause transitions with $f \sim 10^{-4}$. The $F(\Gamma_{ui})$ have never been needed before since we have always used a t_2^3 state for the initial state. Therefore it is not clear how large they will be.

Thus one can conclude that the strength of the ${}^2E \rightarrow {}^2A_1$ transition in ruby is consistent with predictions based on the strength of other transitions. The ${}^2E \rightarrow {}^2A_2$ transition is anomalously large in both ruby and emerald and cannot be explained by this simple theory. This large strength probably comes from high-order mixing with the $c {}^2T_2$ level by an operator which preserves the polarization. Presumably this operator must be the trigonal field rather than the spin-orbit interaction.

2. MgO:Cr³⁺

The theory for MgO:Cr³⁺ follows the same lines as the theory for ruby and emerald. Transitions are not expected in the cubic system except through odd-parity phonons. Thus a ${}^2E \rightarrow {}^2A_2$ no-phonon line is not expected for the cubic system. This is confirmed by experiment.

For the tetragonal pair and vacancy systems, no coupling to the excited bands can occur via the tetragonal field. Terms 2 and 3 in Fig. 18 should be similar to ruby. Hence, they can be neglected also. The ${}^2E \rightarrow {}^2A_2$ transition therefore must be allowed via term 4. With a T_{1u} field only one transition ${}^2E(u) \rightarrow {}^2A_2$ is allowed in π polarization [2A_1 transitions can occur only from the $2E(v)$ state]. This explains why only one line was seen in the weakly doped sample. Again we cannot experimentally confirm the polarized nature of the transition because the axes are randomly oriented. (This would be a particularly interesting case for a polarized excitation experiment.)

We cannot be sure whether the 3819.5-Å or the 3825.3-Å line corresponds to the major pair system with the 7034-Å R line. However, the lack of a 91-cm⁻¹ splitting (the pair system 2E splitting) between any two lines indicates that the pair system has only one line as predicted by theory.

IV. CONCLUSIONS

In summary, we have measured the excited-state absorption spectrum in ruby, emerald, and MgO:Cr³⁺. The sharp I lines (2E , ${}^2T_1 \rightarrow {}^2T_2$) have been seen in all three crystals. Detailed traces of the sharp ${}^2E \rightarrow {}^2A_1$ doublet in ruby and the ${}^2E \rightarrow {}^2A_2$ lines in ruby and MgO:Cr³⁺ have also been

made. In addition, the three excited absorption bands seen are observed with similar strengths in all three crystals.

Energy level calculations and intensity calculations using the closure approximation have been done to confirm the assignments of these transitions. In particular, we have shown that the sharp structure in the MgO:Cr^{3+} spectra arises from the vacancy and pair systems rather than from sites

of cubic symmetry. The agreement between theory and experiment is excellent as to polarization selection rules. Quantitatively the agreement is quite good although small discrepancies exist, as is expected with the closure approximation. The intensity of the ${}^2E \rightarrow {}^2A_1$ transition is explained well, but the ${}^2E \rightarrow {}^2A_2$ transition is more than an order of magnitude stronger than predicted in all three crystals.

†Work supported by the National Science Foundation through the Stanford University Center for Materials Research and through Grant GP-28415.

*Optical Science Center, University of Arizona, Tucson, Ariz. 85721.

‡Molelectron Inc., 177 No. Wolfe Road, Sunnyvale, Calif. 94086.

¹F. Gires and G. Mayer, in *Quantum Electronics* (Columbia, U.P., New York, 1964), p. 841.

²T. Kushida, *J. Phys. Soc. Jpn.* **20**, 619 (1965); **20**, 2312 (1965); **21**, 1331 (1966); *IEEE J. Quant. Electr.* **QE-2**, 534 (1966).

³Y. C. Kiang, J. F. Stephany, and F. C. Unterleitner, *IEEE J. Quant. Electr.* **QE-1**, 295 (1965).

⁴G. K. Klauminzer, P. L. Scott, and H. W. Moos, *Bull. Am. Phys. Soc.* **9**, 706 (1964); *Phys. Rev.* **142**, 248 (1966).

⁵M. Shinada, S. Sugano, and T. Kushida, *J. Phys. Soc. Jpn.* **21**, 1342 (1966).

⁶J. Huang and H. W. Moos, *Phys. Rev.* **173**, 440 (1968).

⁷S. A. Johnson, W. M. Fairbank, Jr., and A. L. Schawlow, *Appl. Opt.* **10**, 2259 (1971).

⁸T. M. Dunn and A. H. Francis, *Phys. Rev. Lett.* **25**, 705 (1970).

⁹Y. Tanabe and H. Kamimura, *J. Phys. Soc. Jpn.* **13**, 394 (1958).

¹⁰W. L. Bragg and J. West, *Proc. R. Soc. (Lond.)* **A111**, 691 (1926).

¹¹N. V. Belov and R. G. Matveeva, *Dokl. Akad. Nauk SSSR* **73**, 299 (1950).

¹²S. Sugano, Y. Tanabe, and H. Kamimura, *Multiplets of Transition-Metal Ions in Crystals* (Academic, New York, 1970).

¹³D. L. Wood, *J. Chem. Phys.* **42**, 3404 (1965).

¹⁴D. L. Wood and K. Nassau, *Am. Mineralogist* **53**, 777 (1968).

¹⁵J. P. Larkin, G. F. Imbusch, and F. Dravnieks, *Phys. Rev. B* **7**, 495 (1973).

¹⁶R. A. Serway, S. A. Marshall, and R. B. Robinson, *Phys. Status Solidi B* **56**, 319 (1973).

¹⁷G. K. Klauminzer (unpublished).

¹⁸W. G. Clark and A. L. Kerlin, *Rev. Sci. Instr.* **38**, 1593 (1967).

¹⁹G. K. Klauminzer, *Appl. Opt.* **9**, 2183 (1970).

²⁰R. L. Aagard and R. A. Dufault, *Appl. Phys. Lett.* **4**, 102 (1964).

²¹T. Nakaya, *Jpn. J. Appl. Phys.* **5**, 79, 689 (1966).

²²A. P. Aleksandrov, V. N. Genkin, and M. I. Kheifets, *Opt. Spectr.* **20**, 69 (1966).

²³V. Denen, C. A. Sacchi, and O. Svelto, *Appl. Opt.* **4**, 863 (1965).

²⁴D. L. Dexter, *Solid State Phys.* **6**, 353 (1958).

²⁵P. Kisliuk and C. A. Moore, *Phys. Rev.* **160**, 307 (1967).

²⁶G. K. Klauminzer, Ph.D. thesis (Stanford University, 1970) (unpublished).

²⁷R. M. Macfarlane, *Phys. Rev. B* **3**, 2129 (1971).

²⁸G. F. Imbusch, Ph.D. thesis (Stanford University, 1964) (unpublished).

²⁹R. M. Macfarlane, *J. Chem. Phys.* **47**, 2066 (1967).

³⁰R. E. Trees, *Phys. Rev.* **82**, 683 (1951); **83**, 756 (1951); **84**, 1089 (1951); **85**, 382 (1952).

³¹J. Ferguson and D. L. Wood, *Australian J. Chem.* **23**, 861 (1970).

³²J. C. Eisenstein, *J. Chem. Phys.* **34**, 1628 (1961).

³³R. M. Macfarlane, *J. Chem. Phys.* **39**, 3118 (1963).

³⁴J. P. Jesson, *J. Chem. Phys.* **48**, 16 (1968).

³⁵W. M. Fairbank, Jr. and G. K. Klauminzer, *Phys. Rev. B* **7**, 500 (1973).

³⁶M. D. Sturge, *Solid State Phys.* **20**, 91 (1967).

³⁷M. Lax, *J. Chem. Phys.* **20**, 1752 (1952).

³⁸S. Sugano and Y. Tanabe, *J. Phys. Soc. Jpn.* **13**, 880 (1958).

³⁹S. Sugano and I. Tsujikawa, *J. Phys. Soc. Jpn.* **13**, 899 (1958).

⁴⁰Configuration interaction cannot account for this large enhancement of the ${}^2T_1 \rightarrow {}^2T_2$ transitions.

⁴¹G. F. Imbusch, A. L. Schawlow, A. D. May, and S. Sugano, *Phys. Rev.* **140**, A830 (1965).

⁴²D. M. Dodd, D. L. Wood, and R. L. Barns, *J. Appl. Phys.* **35**, 1183 (1964).